

---

# Laplacian Eigenfunction-Based Neural Operator for Learning Nonlinear Partial Differential Equations

---

Wenrui Hao<sup>1</sup> Jindong Wang<sup>1</sup>

## Abstract

Learning nonlinear partial differential equations (PDEs) is emerging in many scientific and engineering disciplines, driving advancements in areas such as fluid dynamics, materials science, and biological systems. In this work, we introduce the Laplacian Eigenfunction-Based Neural Operator (LE-NO), a framework for efficiently learning nonlinear terms in PDEs, with a particular focus on nonlinear parabolic equations. By leveraging data-driven approaches to model the right-hand-side nonlinear operator, the LE-NO framework uses Laplacian eigenfunctions as basis functions, enabling efficient approximation of the nonlinear term. This approach reduces the computational complexity of the problem by enabling direct computation of the inverse Laplacian matrix and helps overcome challenges related to limited data and large neural network architectures—common hurdles in operator learning. We demonstrate the capability of our approach to generalize across various boundary conditions and provide insights into its potential applications in mathematical physics. Our results highlight the promise of LE-NO in capturing complex nonlinear behaviors, offering a robust tool for the discovery and prediction of underlying dynamics in PDEs.

## 1. Introduction

With advancements in machine learning techniques and the rapid growth of data, the data-driven discovery of partial differential equations (PDEs) has made significant strides in recent years. Unlike traditional methods that derive physical laws from first principles or constitutive laws, this approach offers an alternative by directly recovering equations from observational data. This is particularly well-suited for systems with complex or elusive underlying mechanisms, such

as those found in biology, where fundamental rules are yet to be fully established.

Initially, the discovery of PDEs was framed as a sparse regression task, selecting a few terms with non-zero coefficients from a vast pool of candidates. Early methods like Lasso (Tibshirani, 1996), sequential threshold ridge regression (Rudy et al., 2017), and SINDy (Brunton et al., 2016) were employed to identify PDEs from predefined candidate libraries. Subsequent research introduced various enhancements to these methods, improving their robustness against noise and their applicability to complex systems (Messenger & Bortz, 2021; Hoffmann et al., 2019; Fasel et al., 2022; Naozuka et al., 2022). However, sparse regression-based methods, while computationally efficient, are constrained by the need for a pre-determined candidate library, which suffers from the curse of dimensionality in high-dimensional systems.

To overcome these limitations, symbolic regression has been employed to relax the constraints, enabling the discovery of free-form PDEs (Kim et al., 2020; Lu et al., 2022; Zhang et al., 2023; Vaddireddy & San, 2019). The rapid development of deep learning has further expanded possibilities, with automatic differentiation in neural networks enhancing the flexibility and accuracy of derivative calculations, particularly in scenarios with sparse and noisy data.

Among neural network-based techniques, physics-informed neural networks (PINNs) (Raissi et al., 2017; 2019; Xu et al., 2023; Zhang & Yang, 2024; Thanasutives et al., 2023; Karniadakis et al., 2021) and operator learning (Hao et al., 2024; Yu et al., 2024) demonstrate exceptional robustness and accuracy in identifying PDEs from sparse and noisy datasets. However, PINNs are computationally intensive, and their accuracy heavily depends on the integration of physical constraints (Krishnapriyan et al., 2021). Most methods discussed have been developed for proof-of-concept studies, often using data derived from numerical solutions of canonical PDEs. While these studies validate the proposed methods, practical applications pose challenges, particularly in verifying the correctness of a discovered PDE when no reference PDE exists.

Existing methods are often sensitive to hyper-parameter se-

<sup>1</sup>Department of Mathematics, The Pennsylvania State University, State College, PA, USA. Correspondence to: Wenrui Hao <wxh64@psu.edu>.

lection, such as regularization magnitudes and thresholds, complicating their practical application where these parameters are difficult to fine-tune without a reference PDE (Wang et al., 2020). An ideal PDE for describing a physical process should satisfy three key principles: precision, parsimony, and interpretability.

To overcome these challenges and reduce the complexity of neural networks, we propose a novel Laplacian Eigenfunctions-Based Neural Operator for learning the nonlinear term of PDEs. This approach integrates the Laplacian kernel with a neural network to model the right-hand side of the PDEs. By leveraging the neural operator, it approximates the differential equation without requiring the neural network to learn the basis functions. The proposed framework is illustrated in Figure 1.

To demonstrate the robustness and accuracy of the proposed approach, we apply it to identify several PDEs from various physical fields. We compare our method with commonly used techniques, such as DeepONet (Lu et al., 2019; 2021) and Fourier Neural Operator (FNO) (Li et al., 2020), highlighting its superiority in terms of neural network size. Additionally, we provide proofs of convergence and analyze the approximation properties of the proposed neural operator. Finally, we apply this new operator to discover previously unrevealed PDEs from MRI data of Alzheimer’s disease patients.

## 2. Laplacian Eigenfunctions-Based Neural Operator

In this section, we will consider the neural operator for learning the nonlinear term of PDEs.

### 2.1. Problem Formulation

We consider the following general nonlinear parabolic PDEs:

$$\begin{cases} u_t - D\Delta u = \mathcal{F}(u), & \text{in } \Omega \times [0, T] \\ u(x, 0) = u_0(x), & \text{in } \Omega \end{cases} \quad (1)$$

Here we consider various boundary conditions:

- Dirichlet Boundary Condition:

$$u = g \quad \text{on } \partial\Omega \times (0, T). \quad (2)$$

- Neumann Boundary Condition:

$$\frac{\partial u}{\partial n} = g \quad \text{on } \partial\Omega \times (0, T). \quad (3)$$

$D$  represents the diffusion coefficient and  $\Omega \subset \mathbb{R}^d$  is a polygonal domain,  $\mathcal{F}$  denotes the nonlinear term determined by empirical data.

The weak form of problem (1) with homogeneous Dirichlet boundary condition reads as: Find  $u \in L^2(0, T; H_0^1(\Omega))$  with  $u_t \in L^2(0, T; H^{-1}(\Omega))$  such that

$$(u_t, v) + (D\nabla u, \nabla v) = (\mathcal{F}(u), v) \quad (4)$$

for  $v \in H_0^1(\Omega)$  with  $u(x, 0) = u_0(x)$ .

The nonlinear term  $\mathcal{F}$  can also be viewed as a nonlinear operator:

$$\mathcal{F} : H^1(\Omega) \rightarrow H^{-1}(\Omega). \quad (5)$$

The primary objective of this paper is the data-driven discovery of the nonlinear term  $\mathcal{F}$  represented by a neural operator,  $\mathcal{N}(u; \theta)$  parameterized by  $\theta$ . This framework is general enough to encompass a wide range of problems in mathematical physics, including pattern formation in biology (Gierer & Meinhardt, 1972), population dynamics (Holmes et al., 1994), catalytic reactions (Gupta & Chakraborty, 2009), and diffusion in alloys (Allen & Cahn, 1975). By leveraging the neural operator, we aim to develop a data-driven model that facilitates efficient prediction and enables the discovery of causal networks underlying their behavior.

### 2.2. Laplacian Eigenfunctions-Based Neural Operator

Given Hilbert spaces  $\mathcal{X}(\Omega), \mathcal{Y}(\Omega)$ , we define the following neural operator

$$\mathcal{N}(\mathbf{u}) = \sum_{i=1}^P \mathcal{A}_i \sigma(\mathcal{W}_i u + \mathcal{B}_i) \quad \forall u \in \mathcal{X}, \quad (6)$$

where  $\mathcal{W}_i \in \mathcal{L}(\mathcal{X}, \mathcal{X})$ : continuous linear operator,  $\mathcal{B}_i \in \mathcal{Y}$ : bias term,  $\mathcal{A}_i \in \mathcal{L}(\mathcal{X}, \mathcal{Y})$ : continuous linear operator, and  $\sigma : \mathbb{R} \rightarrow \mathbb{R}$ : nonlinear pointwise activation function. Normally, the linear operator  $\mathcal{A}_i$  is composed of neural network basis functions, i.e.,

$$\mathcal{A}_i u = \sum_{j=1}^m A_i^j \sigma(\alpha_i^j \cdot x + \zeta_i^j) u, \quad x \in \Omega, u \in \mathcal{X}. \quad (7)$$

where  $A_i^j \in \mathbb{R}$ ,  $\alpha_i^j \in \mathbb{R}^d$  and  $\zeta_i^j \in \mathbb{R}$ . This formulation is designed to learn low-dimensional intrinsic mappings (Lu et al., 2019; Li et al., 2020; He et al., 2023). Since the operator learning involves two neural network representations, the training process becomes quite challenging due to the limited data available, and the architecture itself is also very large.

In this paper, instead of using neural network basis functions, we leverage the eigenfunctions of  $-\Delta$ . Specifically, using the Dirichlet boundary condition with  $g = 0$  as an example, we consider the following eigenvalue problem:

$$\begin{cases} -\Delta \phi_i = \lambda_i \phi_i, & \text{in } \Omega, \\ \phi_i = 0, & \text{on } \partial\Omega, \end{cases} \quad (8)$$

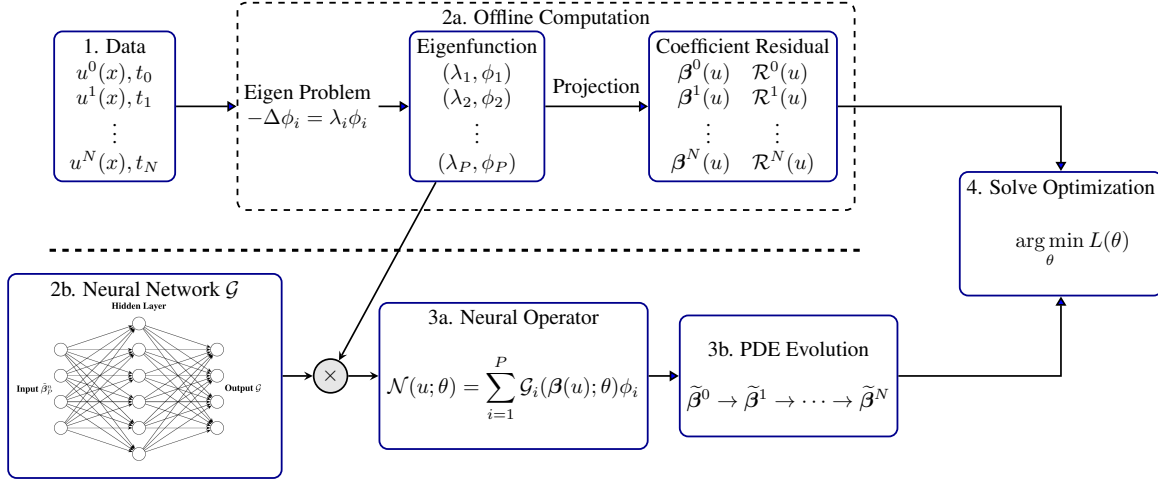


Figure 1. Framework of PDE learning using the Laplacian Eigenfunction-Based Neural Operator (LE-NO). The process involves computing Laplacian eigenfunctions on the domain  $\Omega$ , projecting observed data onto these eigenfunctions to obtain  $\beta^n$  and the residual  $\mathcal{R}^n$ , integrating the eigenfunctions into the neural operator to approximate the nonlinear term of PDEs, and training the neural operator using a loss function based on the PDEs evolution.

with  $\|\phi\|_{L^2(\Omega)} = 1$  and it holds  $0 \leq \lambda_1 \leq \lambda_2 \leq \dots$ .

*Remark 1.* For a rectangular or cubic domain, the eigenfunctions are composed of tensor products of Fourier modes. On an irregular domain, however, eigenfunctions can be derived using discretization methods such as finite element methods. This derivation is performed as an offline preprocessing step to train the neural operator efficiently.

Thus, the Laplacian Eigenfunction-Based Neural Operator is defined as

$$\mathcal{N}(\mathbf{u}) = \sum_{i=1}^P \mathcal{A}_i \sigma(\mathcal{W}_i u + \mathcal{B}_i) \phi_i(x) \quad \forall u \in \mathcal{X}, \quad (9)$$

where it is employed to approximate  $\mathcal{F}$  in Eq. (1) to learn the exact form of the model.

### 2.3. Eigenfunction-Based Method

To learn the nonlinear term in PDEs, we employ a finite-dimensional space spanned by eigenfunctions to accelerate computation. This approach offers two key benefits. First, it eliminates the need for matrix inversion during time evolution, enabling efficient problem-solving and neural network training. Second, the eigenfunctions of the operator serve as basis functions in the neural operator  $\mathcal{N}$ , providing an effective framework for approximating the nonlinear term and diagonalizing the discrete Laplace matrix. This allows for the direct computation of its inverse, further enhancing computational efficiency. We will project both the data and the equation onto the following space:

$$V_P = \text{span}\{\phi_i\}_{i=1}^P. \quad (10)$$

**Data projection:** Given the observed data consisting of data samples  $\{u^n(x), t^n\}_{n=0}^N$  at time  $t_n$ , the projection is defined as:  $\beta_i^n = (u^n(x), \phi_i(x))$ ,  $i = 1, \dots, P$ .

**Equation projection:** By restricting the variational problem (4) to the subspace  $V_P$ , we approximate the numerical solution as  $\tilde{u}_P^n(x) = \sum_{i=1}^P \tilde{\beta}_i^n \phi_i(x)$ .

By applying the semi-implicit Euler method for time discretization and replacing  $\mathcal{F}$  with  $\mathcal{N}$ , we derive the following discrete formulation

$$\frac{\tilde{\beta}^n - \tilde{\beta}^{n-1}}{t_n - t_{n-1}} + D\Lambda_P \tilde{\beta}^n = \mathcal{G}(\tilde{\beta}^{n-1}; \theta), \quad n = 1, \dots, N, \quad (11)$$

where  $\tilde{\beta}^n = (\tilde{\beta}_1^n, \dots, \tilde{\beta}_P^n)^T$ ,  $\Lambda_P = \text{diag}(\lambda_1, \dots, \lambda_P)$ ,  $\mathcal{G}_i = \mathcal{A}_i \sigma(\mathcal{W}_i u + \mathcal{B}_i)$  (due to the orthogonality of  $\phi_i$ ), and  $\mathcal{G} = (\mathcal{G}_1, \dots, \mathcal{G}_P)^T$ . For simplicity, the dependence of  $\tilde{\beta}$  on  $u$  is omitted for simplicity.

**Training Loss:** For simplicity, we denote both the time differentiation operator and the Laplace operator as:

$$\mathcal{R}^n(u) = \frac{\beta^n(u) - \beta^{n-1}(u)}{t_n - t_{n-1}} + D\Lambda_P \beta^n(u). \quad (12)$$

To train the neural network  $\mathcal{G}(\cdot, \theta) : \mathbb{R}^P \rightarrow \mathbb{R}^P$ , we focus on both the data RMSE loss and the model loss:

- Data  $L^2$  loss ensures that the discretized solution  $\tilde{\beta}^n$  closely matches the given data  $\beta^n$ :

$$L^D(\theta) := \frac{1}{N} \sum_{n=1}^N \frac{\|\tilde{\beta}^n - \beta^n\|_{l^2}}{\|\beta^n\|_{l^2}}. \quad (13)$$

- Model residual loss guarantees that the solution satisfies the model problem:

$$L^R(\theta) := \frac{1}{N} \sum_{n=1}^N \frac{\|\mathcal{R}^n - \mathcal{G}(\beta^{n-1}; \theta)\|_{L^2}}{\|\mathcal{R}^n\|_{L^2}}. \quad (14)$$

Then we train the neural operator by minimizing the following combined loss function:

$$\min_{\theta} L(\theta) := L^D(\theta) + L^R(\theta). \quad (15)$$

Thus we summarize the detailed implementation in Algorithm 1 for learning the nonlinear term  $\mathcal{F}$  of the PDE.

---

**Algorithm 1** Learning the nonlinear term of PDEs
 

---

**Input:** Dynamic data samples  $\{u^n(x), t_n\}_{n=0}^N$  at  $t_n$ , domain  $\Omega$  and  $P$ .

- 1: Generate Laplace eigenfunction  $\{\phi_i\}_{i=1}^P$  in  $\Omega$ .
- 2: Project the data samples to compute  $\beta^n$  and residuals  $\mathcal{R}^n$  for all data.
- 3: **for**  $n = 1, \dots, N$  **do**
- 4: Compute  $\tilde{\beta}^n$  using  $\tilde{\beta}^0 = \beta^0$ :

$$\frac{\tilde{\beta}^n - \tilde{\beta}^{n-1}}{t_n - t_{n-1}} + D\Lambda_P \tilde{\beta}^n = \mathcal{G}(\tilde{\beta}^{n-1}; \theta). \quad (16)$$

- 5: **end for**
- 6: Substitute  $\tilde{\beta}^n$  into the loss function  $L$  and optimize the parameters  $\theta$  in the neural operator.

**Output:** The nonlinear term of PDEs,  $\mathcal{N}$ .

---

As illustrated in Figure 1, the framework is specifically designed to learn the complex nonlinear operator  $\mathcal{F}$ .

*Remark 2.* Our method is also applicable to inhomogeneous Dirichlet and Neumann boundary conditions. For detailed discussions and adaptations, refer to Appendix C.

## 2.4. Theoretical Analysis

In this section, we aim to analyze the convergence and the approximation of Laplacian Eigenfunction-Based Neural Operator. The following theorem provides the approximation property for  $\mathcal{N}$ :

**Theorem 1 (operator approximation error).** *Let  $\mathcal{F} : \mathcal{X}(\Omega) \rightarrow \mathcal{Y}(\Omega)$  be a continuous operator with  $\|\mathcal{F}'\| \leq L$ ,  $K \subset \mathcal{X} \cap H^k(\Omega)$  be a compact set and  $\mathcal{F}(K) \subset H^k(\Omega)$ , there exists a neural operator  $\mathcal{N}$  of the form (9), where  $\mathcal{G}$  is a shallow neural network with width  $m$ , such that*

$$\begin{aligned} & \sup_{u \in K} \|\mathcal{N}(u) - \mathcal{F}(u)\|_{L^2(\Omega)} \\ & \leq C(L+1)P^{-\frac{k}{d}} + C \log(m)^{\frac{1}{2}+P} m^{-\frac{1}{P} \frac{P+2}{P+4}}. \end{aligned} \quad (17)$$

where  $C$  is a constant depending on the compact set  $K$ ,

Under this result, we have the following estimate for the approximated solution  $\tilde{u}_P^n$  obtained by the neural operator.

**Theorem 2 (solution approximation error).** *Under assumption in Theorem 1, there exists a neural operator  $\mathcal{N}$  such that*

$$\begin{aligned} & \sup_{0 \leq n \leq N} \|u^n - \tilde{u}_P^n\|_{L^2(\Omega)} \\ & \leq C \sup_{u \in K} \|\mathcal{F}(u) - \mathcal{N}(u)\|_{L^2} T^{1/2} \exp(CLT) \\ & \quad + C(\tau + P^{-\frac{k}{d}}). \end{aligned} \quad (18)$$

where  $\tilde{u}_P^n = \sum_{i=1}^P \tilde{\beta}_i^n \phi_i$ ,  $\tau = \max_n(t_n - t_{n-1})$  and  $\sup_{u \in K} \|\mathcal{F}(u) - \mathcal{N}(u)\|_{L^2}$  can be bounded by the result in Theorem 1.

*Remark 3.* In practice, the available data may have limited regularity, such as belonging to  $L^\infty(\Omega)$ . By the Sobolev embedding theorem (Adams & Fournier, 2003), it holds that  $L^\infty(\Omega) \hookrightarrow H^k(\Omega)$  for  $k < \frac{d}{2}$ , thus the term  $P^{-\frac{k}{d}}$  in (17) and (18) can be replaced by

$$P^{-\frac{k}{d}} \rightarrow P^{-\frac{1}{2}+\xi}, \quad (19)$$

for arbitrary  $\xi > 0$ . For a uniform time step  $\tau = \frac{T}{N}$ , with sufficiently large  $m$ ,  $N$  and  $P$ , the error can be made arbitrarily small.

We explore the convergence behavior of the Laplacian Eigenfunction-Based Neural Operator by analyzing the neural tangent kernel (NTK) (Jacot et al., 2018), which provides estimates of the evolution of the parameter  $\theta(s)$  with respect to  $s$ , as detailed in Appendix B.

**Theorem 3 (training error).** *For a one-step evolution with  $N = 1$  and  $M$  data samples, consider the absolute mean squared loss  $L$  and let  $\mathcal{G}(\circ; \theta)$  be a shallow neural network. In the limit as the width  $m \rightarrow \infty$ , there exists  $s^* > 0$  and  $\gamma_1 > 0$  such that*

$$L(\theta(s)) \leq L(\theta(0)) \exp(-s\tilde{\lambda}_1), \quad (20)$$

for  $s \in [0, s^*]$  with high probability, where  $\tilde{\lambda}_1 = \frac{\gamma_1}{M} (4 + 8 \frac{\tau(1+\tau\lambda_P)^{-1}}{(1+\tau^2(1+\tau\lambda_1)^{-2})})$ .

*Remark 4.* The smallest eigenvalue of the kernel, bounded below by  $\tilde{\lambda}_1$ , relies on the minimum eigenvalue  $\gamma_1$  of the classical NTK for a shallow neural network. Moreover, if we only consider the single loss  $L^R$  for training, as detailed in Appendix B, the corresponding convergence can be expressed as  $L^R(\theta(s)) \leq L^R(\theta(0)) \exp(-s\tilde{\lambda}_1^R)$ , where  $\tilde{\lambda}_1^R = \frac{4\gamma_1}{M}$ . Since  $\tilde{\lambda}_1^R$  is smaller than  $\tilde{\lambda}_1$ , this indicates that employing two different loss functions can accelerate convergence, thereby confirming the efficiency of combining these losses in the training process.

## 3. Numerical Experiments

In this section, we evaluate the effectiveness of the proposed approach by examining several PDE problems in both 1D

and 2D cases. Additionally, we compare the performance of the proposed Laplacian Eigenfunction-Based Neural Operator against several existing neural operators, including FNO and DeepONet. For detailed information on the datasets and the training process, please refer to Appendix D.

The training accuracy is evaluated using three different metrics for  $M$  data samples, as defined below:

- Relative  $L^2$  error of the solution (denoted by  $E_{L^2}$ ):

$$\frac{1}{MN} \sum_{i=1}^M \sum_{n=1}^N \frac{\|(u^n)_i - u_i(t_n)\|_{L^2}}{\|u_i(t_n)\|_{L^2}}$$

- Relative PDE residual error (denoted by  $E_{Res}$ ):

$$\frac{1}{MN} \sum_{m=1}^M \sum_{n=1}^N \frac{\|\mathcal{G}^\theta(\beta^{n-1}(\tilde{u}^n)_i) - \mathcal{R}^n(u_i)\|_{L^2}}{\|\mathcal{R}^n(u_i)\|_{L^2}}$$

- Relative nonlinear term error (denoted by  $E_{Nonlinear}$ ):

$$\frac{1}{MN} \sum_{m=1}^M \sum_{n=1}^N \frac{\|\mathcal{N}((u_P^n)_i) - \mathcal{F}(u_i(t_n))\|_{L^2}}{\|\mathcal{F}(u_i(t_n))\|_{L^2}}$$

These metrics provide a comprehensive assessment of the proposed learning approach's performance in approximating the solution, satisfying the PDE constraints, and accurately capturing the nonlinear terms.

### 3.1. KPP-Fisher Equation

The KPP-Fisher equation is a classic benchmark in reaction-diffusion models, commonly used to describe population growth and wave propagation (Holmes et al., 1994; Fisher, 1937). Its mathematical form in 1D case is given by

$$\begin{cases} \frac{\partial u}{\partial t} - \frac{\partial^2 u}{\partial x^2} = u(1-u), & x \in (0, 1), t \in (0, T] \\ u(x, 0) = u_0(x), & x \in (0, 1) \end{cases} \quad (21)$$

with homogeneous Dirichlet boundary conditions where  $u_0 \in L^2((0, 1); \mathbb{R})$  is the initial condition.

#### 3.1.1. COMPARISON WITH VARIOUS METHODS

The performance of our proposed method, along with comparisons to FNO and DeepONet, is summarized in Table 1. We use  $P = 64$  eigenfunctions to solve the discrete problem (11). For the DeepONet structure used to approximate  $\mathcal{N}$ , we adopt a shallow neural network as the trunk net, while the branch net takes  $\tilde{u}_P^n$  as input and consists of 1,000 neurons. For the FNO structure used for  $\mathcal{N}$ , we employ a 1D FNO with one integral layer, 16 Fourier modes, and a width of 64. Additionally, the loss curves for different methods are

shown in Figure 2. It is noteworthy that the neural operators used in this comparison have parameters of a similar scale.

Our method demonstrates the best performance across all error metrics compared to FNO and DeepONet in Table 1. Furthermore, our approach exhibits remarkable training efficiency, completing one epoch in only 0.03 seconds. This advantage is attributed to its intrinsic and straightforward architecture, which efficiently diagonalizes the linear system for time evolution.

Table 1. Errors comparison between LENO, DeepONet, and FNO on the 1D KPP-Fisher equation.

Method	$E_{L^2}$	$E_{Res}$	$E_{Nonlinear}$	Time/epoch
LENO	5.79e-04	4.56e-03	4.57e-03	0.03s
DeepONet	6.23e-03	5.08e-02	1.83e-01	1.10s
FNO	5.99e-03	1.34e-02	1.28e-02	1.50s

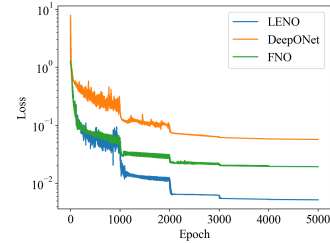


Figure 2. Loss curves of three different neural operators on the KPP-Fisher equation.

#### 3.1.2. COMPARISON WITH DIFFERENT CRITERIA

We also evaluate the performance of the LENO trained with different loss criteria. Table 2 summarizes that training with both  $L^2$  loss ( $L^D$ ) and residual loss ( $L^R$ ) achieves the best performance across all metrics. In contrast, training solely with  $L^2$  loss results in poor learning of the nonlinear term, while incorporating residual loss improves  $L^2$  error as well. These findings suggest that both  $L^2$  and residual errors are necessary in the loss function to ensure balanced and robust performance across all metrics.

Table 2. Errors of different training criteria on the KPP-Fisher equation.

Criterion	$E_{L^2}$	$E_{Res}$	$E_{Nonlinear}$
$L^D + L^R$	5.79e-04	4.56e-03	4.57e-03
$L^R$	1.03e-03	4.98e-03	4.98e-03
$L^D$	4.96e-04	4.70e-01	4.70e-01

#### 3.1.3. PERFORMANCE VERSUS VARIOUS $P$

We evaluate the performance of our method and DeepONet using different numbers of eigenfunctions  $P$  as summarized in Table 3. DeepONet consistently performs worse across all metrics compared to our method. The results indicate that increasing  $P$  generally reduces the error for both



methods. However, when  $P$  becomes very large, the error reduction slows, as it becomes influenced by other factors, such as optimization and discretization errors. To achieve a balance between computational efficiency and accuracy, we recommend using a moderately large  $P$ .

Table 3. Errors versus various  $P$ .

$P$	$E_{L^2}$		$E_{Res}$		$E_{Nonlinear}$	
	Our	DeepONet	Our	DeepONet	Our	DeepONet
2	2.25e-02	1.18e-02	2.09e-02	6.55e-02	2.02e-01	2.66e-01
4	1.81e-03	8.17e-03	4.03e-03	7.33e-02	4.79e-02	1.92e-01
8	5.62e-04	7.47e-03	3.89e-03	7.28e-02	9.17e-03	1.86e-01
16	5.61e-04	6.84e-03	4.20e-03	5.76e-02	4.62e-03	1.83e-01
32	5.81e-04	6.18e-03	4.42e-03	5.08e-02	4.44e-03	1.83e-01
64	5.79e-04	6.23e-03	4.56e-03	5.08e-02	4.57e-03	1.83e-01

### 3.1.4. DYNAMICS PREDICTION RESULTS

We also use our method to predict the solution after training. As shown in Figure 3, we present the  $L^2$ -norm of the solution with respect to time  $t$ . The training process covers the first 10 time steps, represented by the shaded area, while the prediction extends beyond this region. The results demonstrate that our method provides accurate predictions, maintaining consistency with the trained region and effectively predicting to the unknown time steps.

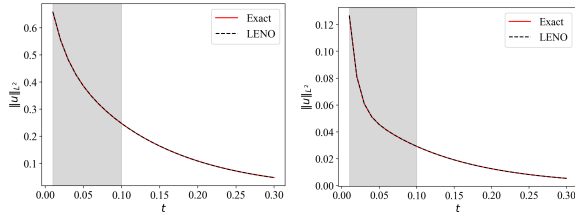


Figure 3. Predicted results ( $L^2$ -norm) for two initial conditions on the KPP-Fisher equation. The shaded area represents the time steps used for training.

### 3.1.5. INHOMOGENEOUS BOUNDARY CONDITION

We also test our method with an inhomogeneous boundary condition:

$$u(0, t) = u(1, t) = 1, \quad t \in (0, T), \quad (22)$$

Our method achieves a performance similar to that observed in the homogeneous setting, namely  $E_{L^2} = 5.56e - 04$ ,  $E_{Res} = 5.27e - 03$ , and  $E_{Nonlinear} = 5.29e - 03$ . The results demonstrate that our method is effective and adaptable to problems with inhomogeneous boundary conditions. Additionally, Figure 4 illustrates that our method delivers accurate predictions of the solution, as evidenced by the  $L^2$ -norm evolution over time. The method generalizes effectively, providing accurate predictions beyond the initial 10 steps of training.

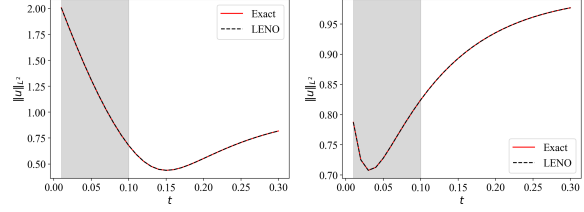


Figure 4. Predicted results ( $L^2$ -norm) for two initial conditions on the KPP-Fisher equation with inhomogeneous boundary condition. The shaded area represents the time steps used for training.

## 3.2. Allen-Cahn Equation

We consider the 1D Allen-Cahn equation which describes the process of phase separation in multi-component alloy systems with a non-flux boundary condition

$$\begin{cases} \frac{\partial u}{\partial t} - \varepsilon^2 \frac{\partial^2 u}{\partial x^2} = W'(u), & x \in (0, 2\pi), t \in (0, T] \\ u(x, 0) = u_0(x), & t \in (0, T) \end{cases} \quad (23)$$

where  $W(u) = \frac{1}{4}(u^2 - 1)^2$  and we set a small diffusion coefficient  $\varepsilon = 0.1$  in this test.

The results of our experiments are presented in Figure 5. In this small diffusion case, our proposed method achieves a similar level of accuracy as in the KPP-Fisher equation. Additionally, we compare the predicted results of our method to those of FNO and DeepONet. We also compare the predicted results of our method to FNO and DeepONet. As shown in Figure 5, DeepONet fails to produce satisfactory results even during the time steps used for training. While FNO shows a good fit during the training steps, its predictions diverge significantly from the true solution within just a few time steps. In contrast, our method maintains reliable prediction accuracy over an extended period, showcasing its ability to generalize and provide stable predictions.

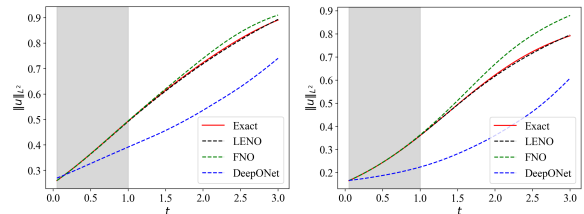


Figure 5. Predicted results ( $L^2$ -norm) for two initial conditions on the Allen-Cahn equation. The shaded area represents the time steps used for training.

## 3.3. Gray-Scott Equations

We consider the following Gray-Scott equations which is a reaction-diffusion system in 1D ( $d = 1$ ) and 2D ( $d = 2$ )

with non-flux boundary conditions:

$$\begin{cases} A_t - D_A \Delta A = SA^2 - (\mu + \rho)A, & x \in \Omega, t \in (0, T) \\ S_t - D_S \Delta S = -SA^2 + \rho(1 - S), & x \in \Omega, t \in (0, T) \\ A(x, 0) = A_0(x) & x \in \Omega \\ S(x, 0) = S_0(x) & x \in \Omega \end{cases} \quad (24)$$

where we set  $\Omega = (0, 2\pi)^d$ ,  $D_A = 2.5 \times 10^{-4}$ ,  $D_S = 5 \times 10^{-4}$ ,  $\rho = 0.04$  and  $\mu = 0.065$ .

### 3.3.1. 1D RESULTS

The quantitative results of error in Table 4 confirm the effectiveness of our approach. Additionally, the predicted results in Figure 6 demonstrate that our method still performs well for a system.

Table 4. Errors of the Gray-Scott equations.

Variable	$E_{L^2}$	$E_{Res}$	$E_{Nonlinear}$
1D Problem			
A	9.55e-04	7.20e-03	8.04e-03
S	9.46e-04	6.50e-03	6.34e-03
2D Problem			
A	5.31e-03	2.32e-02	2.71e-02
S	4.13e-03	1.79e-02	1.66e-02

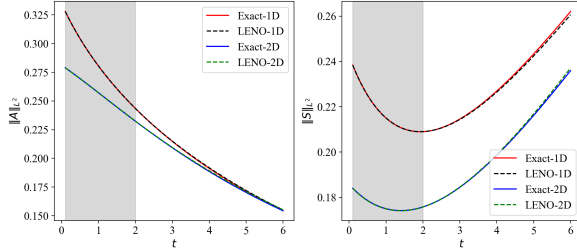


Figure 6. Predicted results ( $L^2$ -norm) of  $A$  (left) and  $S$  (right) on the 1D and 2D Gray-Scott equations. The shaded area represents the first 20 time steps used for training.

### 3.3.2. 2D RESULTS

For the 2D Gray-Scott system, our method achieves slightly lower accuracy compared to the 1D case, as shown in Table 4. However, the performance remains satisfactory, demonstrating the capability of our approach to handle more complex spatial dimensions effectively. The predicted results, presented in Figure 6, further confirm the reliability of our method. Similar to the 1D case, the model provides accurate predictions beyond the training phase, as evidenced by the  $L^2$ -norm evolution for both variables  $A$  and  $S$ . The shaded regions in the plots represent the first 20 time steps used for training, during which the method captures the system dynamics effectively. Beyond these steps, the predictions remain consistent and closely align with the true solutions.

### 3.4. Schrödinger Equation

We consider the following Schrödinger equation with a homogeneous Dirichlet boundary condition:

$$\begin{cases} u_t - \Delta u + \alpha|u|^2 u + Vu = \lambda u, & x \in \Omega, t \in (0, T) \\ u(x, 0) = u_0(x) & x \in \Omega \end{cases} \quad (25)$$

where we set  $\Omega = (-8, 8)^2$ ,  $\alpha = 1600$ ,  $\lambda = 15.87$  is the eigenvalue of the steady problem and the potential is given by:

$$V(x, y) = 100(\sin^2(\frac{\pi x}{4}) + \sin^2(\frac{\pi y}{4})) + x^2 + y^2. \quad (26)$$

This equation features a more complex nonlinear term, which adds to the challenge of accurately solving and predicting the system dynamics. As summarized in Table 7, the results demonstrate that our method achieves low errors, although the difference between the residual error and nonlinear error is slightly larger, reflecting the increased complexity of the nonlinear interactions. Furthermore, Figure 7 illustrates the predicted  $L^2$ -norm evolution over time for the 2D Schrödinger equation. As time progresses, the predicted results show a slight deviation from the actual solution, primarily due to the accumulation of errors over time. This effect becomes more noticeable for such a complex problem. Nevertheless, within the same range of steps as the training phase, our method continues to deliver a good performance.

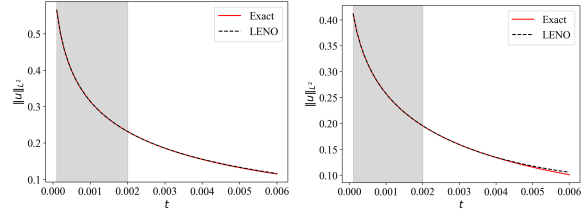


Figure 7. Predicted results ( $L^2$ -norm) for two initial conditions on the 2D Schrödinger equation. The shaded area represents the first 20 time steps used for training.

### 3.5. Alzheimer's Disease Evolution

We analyze the dynamics of cortical thickness in MRI scan slices of Alzheimer's disease patients using the Alzheimer's Disease Neuroimaging Initiative (ADNI) dataset, governed by the following equation:

$$\begin{cases} u_t - D\Delta u = \mathcal{F}(u), & x \in (0, 1)^2, t \in (0, T) \\ u(x, 0) = u_0(x), & x \in (0, 1)^2 \end{cases} \quad (27)$$

with a pure Neumann boundary condition. The diffusion coefficient  $D$  is unknown and is regarded as a parameter in the training. Figure 8 shows MRI scans of a human brain

at three different time points (Baseline, 6 months, and 12 months) for a specific patient. These slices highlight subtle structural changes in the brain over time, potentially indicating the presence of disease or other pathological conditions. By modeling this evolution, we aim to accurately capture these changes through learning the nonlinear term  $\mathcal{F}(u)$ , providing deeper insights into potential abnormalities.

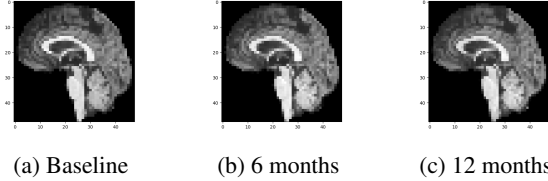


Figure 8. MRI slices of an Alzheimer’s disease patient at three different time points: baseline, 6 months, and 12 months.

Table 8 presents the accuracy results for learning the eigen-coefficients associated with  $L^D$ . The results show that our method achieves an accuracy of at least 90% across all metrics, highlighting its effectiveness in capturing the dynamic behavior. Figure 9 offers a visual comparison between the predicted results and the ground truth, demonstrating a close match.

**Transfer Learning:** We apply transfer learning across different locations for the same patient or different locations across different patients. In this approach, the nonlinear layers of the neural network are kept fixed, with only the linear regression layer being retrained. This allows for efficient adaptation of the model to new spatial regions with minimal training effort. When transferring to a different patient, the time scale may vary due to the heterogeneity among patients. To address this, we introduce a disease progression score  $s = \alpha t + \beta$ , where  $\alpha$  and  $\beta$  are constants (Ghazi et al., 2021; Zheng et al., 2022). The model in (27) becomes:  $\alpha u_t - D\Delta u = \mathcal{N}(u)$  In this case, we use transfer learning to adapt the model for different patients by training the additional parameter  $\alpha$ . Table 5 in the appendix sum-

Table 5. Transfer learning accuracy results (obtained through 10 samples).

Same patient with different positions			
	$1 - L^D$ (%)	$1 - E_{L^2}$ (%)	$1 - E_{Res}$ (%)
avg± std	96.62±1.10	90.47± 2.15	88.21±4.27
Different patients with different positions			
	$1 - L^D$ (%)	$1 - E_{L^2}$ (%)	$1 - E_{Res}$ (%)
avg± std	95.62±3.66	89.63±3.25	92.68±4.33

marizes the transfer learning accuracy for various locations within the same patient, as well as the same locations across different patients. The results demonstrate consistent accuracy ( $\geq 90\%$ ) with previous tests. Figure 9 provides a

visual comparison of the learned and ground truth results for another patient, showing that the outcomes closely align with the true dynamics.

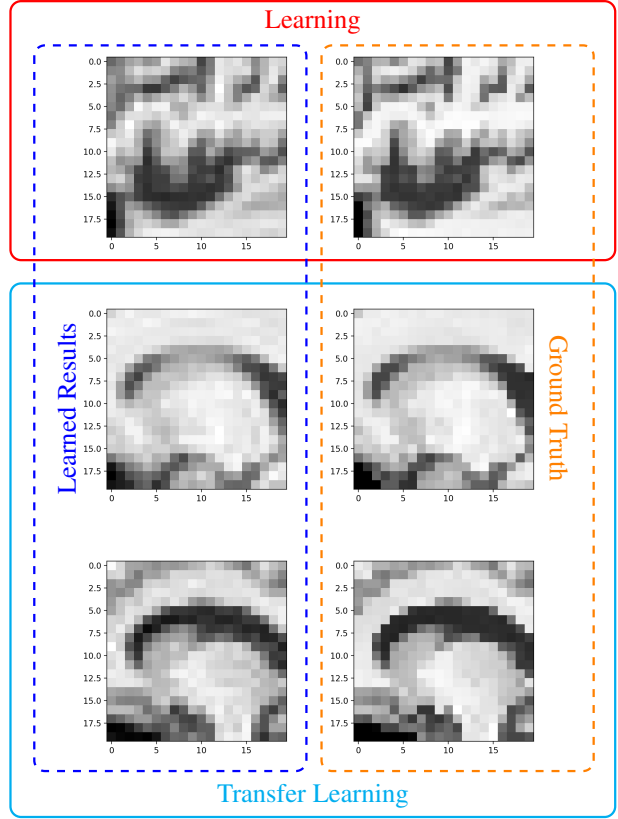


Figure 9. Training result (top), transfer training comparison for the same patient at another position (middle) and different patient (bottom): learned result (left) and ground truth (right).

## 4. Conclusion

This paper presents a Laplacian eigenfunction-based neural operator for learning the nonlinear terms of PDEs in a data-driven manner. By leveraging the eigenfunctions of the Laplace operator as basis functions, the proposed method achieves efficient representation and computation. This approach not only enhances numerical stability but also reduces computational complexity by eliminating the need for matrix inversion during time evolution. The framework provides a robust and generalizable tool for modeling nonlinear phenomena across various domains, including biology, materials science, and population dynamics. Future work will explore extensions to broader classes of PDEs and address challenges related to scalability and data sparsity.

## Acknowledgements

This work was supported by National Institute of General Medical Sciences through grant 1R35GM146894.



## Impact Statement

This paper aims to advance operator learning and model learning for nonlinear PDEs. While our work has numerous potential societal applications in engineering and science, none of them we feel must be specifically highlighted here.

## References

- Adams, R. A. and Fournier, J. J. *Sobolev spaces*. Elsevier, 2003.
- Allen, S. M. and Cahn, J. W. Coherent and incoherent equilibria in iron-rich iron-aluminum alloys. *Acta Metallurgica*, 23(9):1017–1026, 1975.
- Brunton, S. L., Proctor, J. L., and Kutz, J. N. Discovering governing equations from data by sparse identification of nonlinear dynamical systems. *Proceedings of the national academy of sciences*, 113(15):3932–3937, 2016.
- Evans, L. C. *Partial differential equations*, volume 19. American Mathematical Society, 2022.
- Fabian, M., Habala, P., Hájek, P., Montesinos, V., and Zizler, V. *Banach space theory: The basis for linear and nonlinear analysis*. Springer Science & Business Media, 2011.
- Fasel, U., Kutz, J. N., Brunton, B. W., and Brunton, S. L. Ensemble-sindy: Robust sparse model discovery in the low-data, high-noise limit, with active learning and control. *Proceedings of the Royal Society A*, 478(2260): 20210904, 2022.
- Fisher, R. A. The wave of advance of advantageous genes. *Annals of eugenics*, 7(4):355–369, 1937.
- Ghazi, M. M., Nielsen, M., Pai, A., Modat, M., Cardoso, M. J., Ourselin, S., and Sørensen, L. Robust parametric modeling of alzheimer’s disease progression. *Neuroimage*, 225:117460, 2021.
- Gierer, A. and Meinhardt, H. A theory of biological pattern formation. *Kybernetik*, 12:30–39, 1972.
- Gupta, A. and Chakraborty, S. Linear stability analysis of high-and low-dimensional models for describing mixing-limited pattern formation in homogeneous autocatalytic reactors. *Chemical Engineering Journal*, 145(3):399–411, 2009.
- Hao, W., Liu, X., and Yang, Y. Newton informed neural operator for computing multiple solutions of nonlinear partials differential equations. *arXiv preprint arXiv:2405.14096*, 2024.
- He, J., Liu, X., and Xu, J. Mgno: Efficient parameterization of linear operators via multigrid. *arXiv preprint arXiv:2310.19809*, 2023.
- Hoffmann, M., Fröhner, C., and Noé, F. Reactive sindy: Discovering governing reactions from concentration data. *The Journal of chemical physics*, 150(2), 2019.
- Holmes, E. E., Lewis, M. A., Banks, J., and Veit, R. Partial differential equations in ecology: spatial interactions and population dynamics. *Ecology*, 75(1):17–29, 1994.
- Jacot, A., Gabriel, F., and Hongler, C. Neural tangent kernel: Convergence and generalization in neural networks. *Advances in neural information processing systems*, 31, 2018.
- Karniadakis, G. E., Kevrekidis, I. G., Lu, L., Perdikaris, P., Wang, S., and Yang, L. Physics-informed machine learning. *Nature Reviews Physics*, 3(6):422–440, 2021.
- Kim, S., Lu, P. Y., Mukherjee, S., Gilbert, M., Jing, L., Čeperić, V., and Soljačić, M. Integration of neural network-based symbolic regression in deep learning for scientific discovery. *IEEE transactions on neural networks and learning systems*, 32(9):4166–4177, 2020.
- Krishnapriyan, A., Gholami, A., Zhe, S., Kirby, R., and Mahoney, M. W. Characterizing possible failure modes in physics-informed neural networks. *Advances in neural information processing systems*, 34:26548–26560, 2021.
- Li, Z., Kovachki, N., Azizzadenesheli, K., Liu, B., Bhattacharya, K., Stuart, A., and Anandkumar, A. Fourier neural operator for parametric partial differential equations. *arXiv preprint arXiv:2010.08895*, 2020.
- Lu, L., Jin, P., and Karniadakis, G. E. DeepoNet: Learning nonlinear operators for identifying differential equations based on the universal approximation theorem of operators. *arXiv preprint arXiv:1910.03193*, 2019.
- Lu, L., Jin, P., Pang, G., Zhang, Z., and Karniadakis, G. E. Learning nonlinear operators via deepoNet based on the universal approximation theorem of operators. *Nature machine intelligence*, 3(3):218–229, 2021.
- Lu, P. Y., Ariño Bernad, J., and Soljačić, M. Discovering sparse interpretable dynamics from partial observations. *Communications Physics*, 5(1):206, 2022.
- Mao, T. and Zhou, D.-X. Rates of approximation by relu shallow neural networks. *Journal of Complexity*, 79: 101784, 2023.
- Messenger, D. A. and Bortz, D. M. Weak sindy for partial differential equations. *Journal of Computational Physics*, 443:110525, 2021.
- Naozuka, G. T., Rocha, H. L., Silva, R. S., and Almeida, R. C. Sindy-sa framework: enhancing nonlinear system identification with sensitivity analysis. *Nonlinear Dynamics*, 110(3):2589–2609, 2022.

- Raissi, M., Perdikaris, P., and Karniadakis, G. E. Physics informed deep learning (part i): Data-driven solutions of nonlinear partial differential equations. *arXiv preprint arXiv:1711.10561*, 2017.
- Raissi, M., Perdikaris, P., and Karniadakis, G. E. Physics-informed neural networks: A deep learning framework for solving forward and inverse problems involving nonlinear partial differential equations. *Journal of Computational physics*, 378:686–707, 2019.
- Rudy, S. H., Brunton, S. L., Proctor, J. L., and Kutz, J. N. Data-driven discovery of partial differential equations. *Science advances*, 3(4):e1602614, 2017.
- Thanasutives, P., Morita, T., Numao, M., and Fukui, K.-i. Noise-aware physics-informed machine learning for robust pde discovery. *Machine Learning: Science and Technology*, 4(1):015009, 2023.
- Tibshirani, R. Regression shrinkage and selection via the lasso. *Journal of the Royal Statistical Society Series B: Statistical Methodology*, 58(1):267–288, 1996.
- Vaddireddy, H. and San, O. Equation discovery using fast function extraction: a deterministic symbolic regression approach. *Fluids*, 4(2):111, 2019.
- Wang, S., Teng, Y., and Perdikaris, P. Understanding and mitigating gradient pathologies in physics-informed neural networks. *arXiv preprint arXiv:2001.04536*, 2020.
- Xu, H., Zeng, J., and Zhang, D. Discovery of partial differential equations from highly noisy and sparse data with physics-informed information criterion. *Research*, 6:0147, 2023.
- Yang, Y., Chen, Q., and Hao, W. Homotopy relaxation training algorithms for infinite-width two-layer relu neural networks. *Journal of Scientific Computing*, 102(2):40, 2025.
- Yu, Y., Liu, N., Lu, F., Gao, T., Jafarzadeh, S., and Silling, S. Nonlocal attention operator: Materializing hidden knowledge towards interpretable physics discovery. *arXiv preprint arXiv:2408.07307*, 2024.
- Zhang, B. and Yang, C. Discovering physics-informed neural networks model for solving partial differential equations through evolutionary computation. *Swarm and Evolutionary Computation*, 88:101589, 2024.
- Zhang, M., Kim, S., Lu, P. Y., and Soljačić, M. Deep learning and symbolic regression for discovering parametric equations. *IEEE Transactions on Neural Networks and Learning Systems*, 2023.
- Zheng, H., Petrella, J. R., Doraiswamy, P. M., Lin, G., Hao, W., and Initiative, A. D. N. Data-driven causal model discovery and personalized prediction in alzheimer’s disease. *NPJ digital medicine*, 5(1):137, 2022.

## A. Convergence Results

To analyze the approximation properties of the neural operator  $\mathcal{N}$ , we consider a sequence of basis functions  $\{\phi_i^{\mathcal{X}}\}$  of a general Hilbert space  $\mathcal{X}$  satisfying the following approximation property:

$$\lim_{n \rightarrow \infty} \inf_{v_n \in \text{span}\{\phi_i^{\mathcal{X}}\}_{i=1}^n} \|v - v_n\|_{\mathcal{X}} = 0, \quad (28)$$

for all  $v \in \mathcal{X}$ . We define  $T_n^{\mathcal{X}}$  as the projection operators on  $\text{span}\{\phi_i^{\mathcal{X}}\}_{i=1}^n$ .

Then given Hilbert spaces  $\mathcal{X}, \mathcal{Y}$  and a nonlinear operator  $\mathcal{F} : \mathcal{X} \rightarrow \mathcal{Y}$ , if these spaces have projection operators  $T_n^{\mathcal{X}}, T_n^{\mathcal{Y}}$  associated with basis  $\phi_i^{\mathcal{X}} \in \mathcal{X}, \phi_i^{\mathcal{Y}} \in \mathcal{Y}$ , respectively. For a fixed integer  $n$ , we define an approximation operator for  $\mathcal{F}$  as

$$\mathcal{F}_n(u) := T_n^{\mathcal{Y}} \circ \mathcal{F} \circ T_n^{\mathcal{X}}(u) \quad (29)$$

Rewriting  $T_n^{\mathcal{Y}}u$  as a linear combination of the basis  $\{\phi_i^{\mathcal{Y}}\}_{i=1}^n$ , we have

$$T_n^{\mathcal{Y}}y = \sum_{i=1}^n \alpha_i^{\mathcal{Y}}(y) \phi_i^{\mathcal{Y}}, \quad y \in \mathcal{Y}, \quad (30)$$

where  $\alpha_i^{\mathcal{Y}}(y)$  are linear continuous functionals. The approximation operator  $\mathcal{F}_n$  can then be expressed as

$$\mathcal{F}_n(u) = \sum_{j=1}^n \alpha_j^{\mathcal{Y}}(\mathcal{F} \circ T_n^{\mathcal{X}}u) \phi_j^{\mathcal{Y}}. \quad (31)$$

Further, we rewrite  $T_n^{\mathcal{X}}u$  as a linear combination of  $\phi_i^{\mathcal{X}}$

$$T_n^{\mathcal{X}}u = \sum_{i=1}^n \alpha_i^{\mathcal{X}}(u) \phi_i^{\mathcal{X}}, \quad u \in \mathcal{X}. \quad (32)$$

The coefficient part is given by

$$\alpha_j^{\mathcal{Y}}(\mathcal{F} \circ T_n^{\mathcal{X}}u) = \alpha_j^{\mathcal{Y}}(\mathcal{F} \circ \sum_{i=1}^n \alpha_i^{\mathcal{X}}(u) \phi_i^{\mathcal{X}}). \quad (33)$$

Here,  $\alpha_j^{\mathcal{Y}}(\mathcal{F} \circ \sum_{i=1}^n \alpha_i^{\mathcal{X}}(u) \phi_i^{\mathcal{X}})$  can be viewed as a function of  $\alpha_i^{\mathcal{X}}(u)$ . We define

$$\mathcal{G}_j(\alpha_1^{\mathcal{X}}(u), \dots, \alpha_n^{\mathcal{X}}(u)) := \alpha_j^{\mathcal{Y}}(\mathcal{F} \circ \sum_{i=1}^n \alpha_i^{\mathcal{X}}(u) \phi_i^{\mathcal{X}}), \quad (34)$$

where  $\mathcal{G}_j$  is clearly a continuous function.

If we use a neural network to approximate  $\mathcal{G}_j$  such that

$$\mathcal{G}_j(\cdot) \sim \sum_{i=1}^m \mathcal{A}_j^i \sigma(\omega_j^i \cdot + b_j^i),$$

for some  $\omega_j \in \mathbb{R}^n$  and  $b_j^i \in \mathbb{R}$ , we obtain the following neural operator

$$\mathcal{N}(u) := \sum_{i=1}^n \sum_{j=1}^m (A_j^i \phi_i^{\mathcal{Y}}) \sigma(\omega_j^i \cdot \alpha_n^{\mathcal{X}}(u) + b_j^i). \quad (35)$$

where  $\alpha_n^{\mathcal{X}}(u) = (\alpha_1^{\mathcal{X}}(u), \dots, \alpha_n^{\mathcal{X}}(u))^T$ .

Here

- $\mathcal{W}_j^i u := \omega_j^i \cdot \alpha_n^{\mathcal{X}}(u)$  is a linear continuous operator on  $\mathcal{X}$ .

- $\mathcal{B}_j^i := b_j^i \in \mathcal{X}$  is a bias term.
- $\mathcal{A}_j^i u := A_j^i \phi_i^{\mathcal{Y}} u$ ,  $u \in \mathcal{X}$  is a continuous linear operator from  $\mathcal{X}$  to  $\mathcal{Y}$ .

If we sum the two summations together with  $P = nm$ , the neural operator can be rewritten in the compact form shown in (6)

$$\mathcal{N}(u) = \sum_{i=1}^P \mathcal{A}_i \sigma(\mathcal{W}_i u + \mathcal{B}_i) \quad (36)$$

Specifically, when using a neural network as the basis  $\phi_i^{\mathcal{Y}}$ , the operator  $\mathcal{A}_i$  takes the form shown in (7).

To provide an approximation result for  $\mathcal{N}$ , it suffices to analyze the approximation properties of  $\mathcal{F}_n$ . Since the difference between  $\mathcal{N}$  and  $\mathcal{F}_n$  can be made arbitrarily small by choosing a sufficiently wide neural network (large  $m$ ), which is guaranteed by the universal approximation property of neural networks.

To begin with, we consider an extended set for the approximation result, defined as:

$$\widehat{K} = K \cup \overline{\bigcup_{j=1}^{\infty} T_j^{\mathcal{X}}(K)}. \quad (37)$$

We now establish the compactness of the extended set  $\widehat{K}$ .

**Lemma 4** (compactness of extended set). *The extended set  $\widehat{K}$  given in (37) is compact.*

*Proof.* Since  $T_n^{\mathcal{X}}$  is linear continuous, it is uniformly continuous on the compact set  $K$ . For any  $r > 0$ , there exists  $N \in \mathbb{N}$  such that

$$\sup_{u \in \mathcal{X}} \|u - T_j^{\mathcal{X}} u\|_{\mathcal{X}} < r/2,$$

for  $j \geq N$ . Now, cover  $K$  by finite balls of radius  $r/2$  and let  $z_1, \dots, z_l$  be the centers of these balls. Then balls of radius  $r$  around  $z_1, \dots, z_l$  cover

$$K \cup \bigcup_{j=N}^{\infty} T_j^{\mathcal{X}}(K), \quad (38)$$

since for any  $z \in K$ , there exists  $z_l$  such that  $\|z - z_l\|_{\mathcal{X}} < r/2$  and

$$\|T_j^{\mathcal{X}}(z) - z_l\|_{\mathcal{X}} \leq \|T_j^{\mathcal{X}}(z) - z\|_{\mathcal{X}} + \|z - z_l\|_{\mathcal{X}} \leq r/2 + r/2 < r. \quad (39)$$

The remaining set

$$S = \bigcup_{j=1}^{N-1} T_j^{\mathcal{X}}(K), \quad (40)$$

is a finite union of images of the compact set  $K$  under the linear operators  $T_j^{\mathcal{X}}$ , and is therefore compact. Thus it can also be covered by finitely many balls of radius  $r$ . Since  $r > 0$  is arbitrary and  $\widehat{K}$  is closed, the compactness follows.  $\square$

First, we consider using the projection operator  $\Pi_P$  on  $V_P$  to give the specific formulation  $\mathcal{F}_P = \Pi_P \circ \mathcal{F} \circ \Pi_P$ . The following theorem establishes the approximation property for  $\mathcal{F}_P$ .

**Lemma 5.** *Let  $\mathcal{F} : \mathcal{X}(\Omega) \cap H^k(\Omega) \subset \mathcal{Y}(\Omega)$  be a Lipschitz continuous operator with constant  $L$ ,  $K \subset U$  be a compact set and  $\mathcal{F}(K) \subset H^k(\Omega)$ , it holds that*

$$\sup_{u \in K} \|\mathcal{F}_P(u) - \mathcal{F}(u)\|_{L^2} \leq C(L+1)P^{-\frac{k}{d}}. \quad (41)$$

given  $P \in \mathbb{N}$ .

*Proof.* Substituting the formulation of  $\mathcal{F}_P$ , we have

$$\|\mathcal{F}(u) - \Pi_P \circ \mathcal{F} \circ \Pi_P(u)\|_{L^2} \leq \|\mathcal{F}(u) - \Pi_P \circ \mathcal{F}(u)\|_{L^2} + \|\Pi_P \circ (\mathcal{F}(u) - \mathcal{F} \circ \Pi_P(u))\|_{L^2},$$

Since  $\Pi_P$  is linear continuous operator and  $\mathcal{F}$  is a continuous operator, the set  $\mathcal{F}(K)$  is also compact. By the approximation property of the basis  $\phi_i$ , it holds that

$$\|\Pi_P v - v\|_{L^2} \leq CP^{-\frac{k}{d}}, \quad \forall v \in \mathcal{F}(K).$$

Refer to (Fabian et al., 2011, Theorem 4.10), the projection operators are uniform bounded, i.e., there exists  $C$  independent of  $P$  such that

$$\|\Pi_P\| \leq C.$$

Thus, we have :

$$\begin{aligned} \|\Pi_P \circ (\mathcal{F}(u) - \mathcal{F} \circ \Pi_P(u))\|_{L^2} &\leq C\|\mathcal{F}(u) - \mathcal{F} \circ \Pi_P(u)\|_{L^2} \\ &\leq CL\|u - \Pi_P(u)\|_{L^2} \\ &\leq CLP^{-\frac{k}{d}}. \end{aligned}$$

Collecting the above results, we achieve the desired results.  $\square$

Combining the above results, we now provide the proof of Theorem 1.

*proof of Theorem 1.* Using the triangle inequality, we have

$$\|\mathcal{N}(u) - \mathcal{F}(u)\|_{\mathcal{Y}} \leq \|\mathcal{N}(u) - \mathcal{F}_P(u)\|_{L^2} + \|\mathcal{F}_P(u) - \mathcal{F}(u)\|_{L^2}$$

As shown in Lemma 5, we have

$$\sup_{u \in K} \|\mathcal{F}_P(u) - \mathcal{F}(u)\|_{\mathcal{Y}} \leq C(L+1)P^{-\frac{k}{d}}.$$

Meanwhile, recalling the definition of the continuous function  $\mathcal{G}_j$  in (34), we can express

$$\mathcal{F}_P(u) - \mathcal{N}(u) = \sum_{j=1}^P (\mathcal{G}_j(\beta(u)) - \mathcal{G}_j(\beta(u); \theta)) \phi_j,$$

where  $\mathcal{G}_j(\cdot; \theta)$  is defined as

$$\mathcal{G}_j(\circ; \theta) := \sum_{i=1}^W A_j^i \sigma(\omega_j^i \cdot \circ + b_j^i)$$

with  $\omega_j^i \in \mathbb{R}^P$ ,  $A_j^i, b_j^i \in \mathbb{R}$  and  $\beta(u) = ((\phi_1, u), \dots, (\phi_P, u))^T$ .

Since  $\mathcal{F}'$  is bounded, it follows from the definition that  $\mathcal{G}_j \in W^{1, \infty}$ . Consider ReLU as activation function, using (Mao & Zhou, 2023, Theorem 1), it holds that

$$\|\mathcal{G}_j - \mathcal{G}_j^\theta\|_{L^\infty} \leq C\|\mathcal{G}_j\|_{W^{1, \infty}} \log(m)^{\frac{1}{2}+P} m^{-\frac{1}{P} \frac{P+2}{P+4}}.$$

This implies

$$\sup_{u \in K} \|\mathcal{F}_P(u) - \mathcal{N}(u)\|_{L^2} \leq C \left( \sum_{j=1}^P \|\mathcal{G}_j\|_{W^{1, \infty}}^2 \right)^{1/2} \log(m)^{\frac{1}{2}+P} m^{-\frac{1}{P} \frac{P+2}{P+4}}.$$

Note that

$$\begin{aligned} \sum_{j=1}^P \|\mathcal{G}_j(\beta(u))\|_{W^{1, \infty}}^2 &\leq \sum_{j=1}^{\infty} \|\mathcal{G}_j(\beta(u))\|_{W^{1, \infty}}^2 \\ &= \sup_{u \in K} \sum_{j=1}^{\infty} |\mathcal{G}_j'(\beta(u))|^2 + |\mathcal{G}_j(\beta(u))|^2 \\ &= \sup_{u \in K} \left\| \sum_{j=1}^{\infty} \mathcal{G}_j'(\beta(u)) \phi_j \right\|_{L^2}^2 + \left\| \sum_{j=1}^{\infty} \mathcal{G}_j(\beta(u)) \phi_j \right\|_{L^2}^2 \\ &= \sup_{u \in K} \|\mathcal{F}'(\Pi_P u)\|_{L^2}^2 + \|\mathcal{F}(\Pi_P u)\|_{L^2}^2 \leq C(K, L), \end{aligned}$$



for some constant  $C$  depends on compact set  $K$  since  $\mathcal{F}$  is uniform continuous and  $\|\mathcal{F}'\| \leq L$ . In this way, we have

$$\sup_{u \in K} \|\mathcal{F}_P(u) - \mathcal{N}(u)\|_{L^2} \leq C \log(m)^{\frac{1}{2}+P} m^{-\frac{1}{P} \frac{P+2}{P+4}}.$$

Combining the above results, we obtain

$$\sup_{u \in K} \|\mathcal{N}(u) - \mathcal{F}(u)\|_{L^2} \leq C(L+1)P^{-\frac{k}{d}} + C \log(m)^{\frac{1}{2}+P} m^{-\frac{1}{P} \frac{P+2}{P+4}}.$$

□

Now, to analyze the error of the approximate solution  $\tilde{u}_P^n$ , we consider the continuous variation problem of using neural operator  $\mathcal{N}$  to approximate  $\mathcal{F}$ , which gives the following problem: Find  $\tilde{u} \in L^2(0, T; H_0^1(\Omega))$  with  $\tilde{u}_t \in L^2(0, T; H^{-1}(\Omega))$  such that

$$(\tilde{u}_t, v) + (D\nabla\tilde{u}, \nabla v) = (\mathcal{N}(\tilde{u}), v) \quad t \in (0, T), \quad \forall v \in H_0^1(\Omega). \quad (42)$$

for  $v \in H_0^1(\Omega)$  with  $\tilde{u}(x, 0) = u_0(x)$ .

**Lemma 6.** *Let  $u$  be the solution of (1) and  $\tilde{u}$  be the solution of (42). Under the assumption of Theorem 1, we have the following estimate*

$$\sup_{0 \leq t \leq T} \|u(t) - \tilde{u}(t)\|_{H_0^1(\Omega)} \leq C \sup_u \|\mathcal{F}(u) - \mathcal{N}(u)\|_{L^2} T^{1/2} \exp(CLT). \quad (43)$$

*Proof.* Following the regularity results of elliptic equations (Evans, 2022), the following inequality holds:

$$\begin{aligned} \sup_{0 \leq t \leq T} \|u(t) - \tilde{u}(t)\|_{H^1(\Omega)} &\leq C \|\mathcal{F}(u) - \mathcal{N}(\tilde{u})\|_{L^2(0, T; L^2(\Omega))} \\ &\leq C \|\mathcal{F}(\tilde{u}) - \mathcal{N}(\tilde{u})\|_{L^2(0, T; L^2(\Omega))} + C \|\mathcal{F}(u) - \mathcal{F}(\tilde{u})\|_{L^2(0, T; L^2(\Omega))} \\ &\leq CT^{1/2} \sup_u \|\mathcal{F}(u) - \mathcal{N}(u)\|_{L^2} + CL \|u - \tilde{u}\|_{L^2(0, T; L^2(\Omega))} \\ &\leq CT^{1/2} \sup_u \|\mathcal{F}(u) - \mathcal{N}(u)\|_{L^2} + CL \|u - \tilde{u}\|_{L^2(0, T; H_0^1(\Omega))}, \end{aligned} \quad (44)$$

Utilizing Gronwall's inequality on the above result, we obtain

$$\sup_{0 \leq t \leq T} \|u(t) - \tilde{u}(t)\|_{H^1(\Omega)} \leq C \sup_u \|\mathcal{F}(u) - \mathcal{N}(u)\|_{L^2} T^{1/2} \exp(CLT). \quad (45)$$

□

*Remark 5.* This theorem highlights that the error may grow as time progresses. To achieve a more accurate solution using the neural operator, it is essential for the neural operator to provide a more precise approximation of the nonlinear term.

Consider time step  $t_n = n\tau$  ( $n = 0, 1, \dots, N$ ) be a uniform partition of  $[0, T]$  with  $\tau = T/N$ , we then use semi-implicit Euler scheme for time discretization of (42): find  $\tilde{u}^n(x) \in H_0^1(\Omega)$  such that

$$\left(\frac{\tilde{u}^n - \tilde{u}^{n-1}}{\tau}, v\right) + (D\nabla\tilde{u}^n, \nabla v) = (\mathcal{N}(\tilde{u}^{n-1}), v), \quad (46)$$

for any  $v \in H_0^1(\Omega)$  and  $n = 1, 2, \dots, N$  with  $\tilde{u}^0(x) = u^0(x)$ .

For the discrete variational problem, the approximation property of the space  $V_P$  is: Let  $u \in H^k(\Omega) \cap H_0^1(\Omega)$ , it holds that

$$\min_{u_P \in V_P} \|u - u_P\|_{L^2} = \mathcal{O}(P^{-\frac{k}{d}}). \quad (47)$$

Through careful analysis under the regularity requirements for  $\mathcal{N}$ , we can derive the following estimate.

**Lemma 7.** *Let  $\tilde{u}$  be solution of (42) satisfying  $\tilde{u} \in L^2(0, T; H_0^1(\Omega)) \cap L^2(0, T; H^k(\Omega))$  and  $\tilde{u}_P^n$  be solution of (42) restricted on  $V_P$ , it holds that*

$$\sup_{0 \leq n \leq N} \|\tilde{u}^n - \tilde{u}_P^n\|_{L^2(\Omega)} \leq C(\tau + P^{-\frac{k}{d}}). \quad (48)$$

where  $C$  is independent of  $\tau$  and  $P$ .

*Proof.* Consider  $w_P$  as the elliptic projection in  $V_P$  of the exact solution  $\tilde{u}$ , defined as:

$$(\nabla w_P, v_P) = (\tilde{u}, v_P), \quad \forall v_P \in V_P. \quad (49)$$

This allows us to express the error as the sum of two terms

$$\tilde{u}_P - \tilde{u} = (u_P - w_P) + (w_P - \tilde{u}) := \theta + \rho. \quad (50)$$

It follows that, for any  $\chi \in V_P$

$$\|\nabla(w_P - \tilde{u})\|^2 = (\nabla(w_P - \tilde{u}), \nabla(\chi - \tilde{u})) \leq \|\nabla(w_P - \tilde{u})\| \|\nabla(\chi - \tilde{u})\|, \quad (51)$$

Using the approximation property of  $V_P$ , we obtain

$$\|\nabla(w_P - \tilde{u})\| \leq CP^{-\frac{k-1}{d}} \|\tilde{u}\|_{H^k}. \quad (52)$$

By a duality argument, consider solving the problem

$$-\Delta\psi = \phi \text{ in } \Omega, \quad \psi = 0 \text{ on } \partial\Omega. \quad (53)$$

We then have:

$$\|\nabla\psi\|^2 = (\phi, \psi) \leq \|\phi\| \|\psi\| \leq C\|\phi\| \|\nabla\psi\|, \quad (54)$$

where the Poincaré inequality is applied. Using elliptic regularity, we further deduce:

$$\|\psi\|_2 \leq C\|\phi\| \quad (55)$$

We have

$$\begin{aligned} (w_P - \tilde{u}, \phi) &= (\nabla(w_P - \tilde{u}), \nabla\psi) \\ &= (\nabla(w_P - \tilde{u}), \nabla(\psi - \chi)) \\ &\leq \|\nabla(w_P - \tilde{u})\| \|\nabla(\psi - \chi)\| \leq CP^{-\frac{k}{d}} \|\psi\|_2 \|u\|_k \\ &\leq CP^{-\frac{k}{d}} \|\phi\| \|u\|_k. \end{aligned} \quad (56)$$

Taking  $\phi = w_P - \tilde{u}$ , we derive the estimate for  $\rho = w_P - \tilde{u}$

$$\|\rho\| \leq C(\tilde{u})P^{-\frac{k}{d}}. \quad (57)$$

With a similar induction, we obtain

$$\|\rho_t\| \leq C(\tilde{u})P^{-\frac{k}{d}}. \quad (58)$$

Let  $w_P^n = w_P(t_n)$  and  $\tilde{u}^n = \tilde{u}(t_n)$ , we can rewrite

$$\tilde{u}_P^n - \tilde{u}^n = (\tilde{u}_P^n - w_P^n) + (w_P^n - \tilde{u}^n) := \theta^n + \rho^n. \quad (59)$$

It follows that:

$$\begin{aligned} &(\bar{\partial}\theta^n, \chi) + (\nabla\theta^n, \nabla\chi) \\ &= (\mathcal{N}(\tilde{u}_P^{n-1}) - \mathcal{N}(\tilde{u}^n), \chi) - (\bar{\partial}\rho^n, \chi) - (\bar{\partial}\tilde{u}^n - \tilde{u}_P^n, \chi), \end{aligned} \quad (60)$$

where  $\bar{\partial}\theta^n = \frac{\theta^n - \theta^{n-1}}{\tau}$ .

Using the continuity of  $\mathcal{N}$ , we have

$$\|\mathcal{N}(\tilde{u}_P) - \mathcal{N}(\tilde{u}^n)\| \leq C\|\tilde{U}_M^{n-1} - \tilde{u}^n\| \leq C(\|\theta^{n-1}\| + \|\rho^{n-1}\| + \tau\|\bar{\partial}\tilde{u}^n\|). \quad (61)$$

For  $\chi = \theta^n$ , we have

$$\frac{1}{2}\bar{\partial}\|\theta^n\|^2 + \|\theta^n\|^2 \leq C(\|\theta^{n-1}\| + \|\rho^{n-1}\| + \tau\|\bar{\partial}\tilde{u}^n\| + \|\bar{\partial}\rho^n\| + \|\bar{\partial}\tilde{u}^n - \tilde{u}_t^n\|)\|\theta^n\|. \quad (62)$$

After kicking back  $\|\nabla\theta^n\|$ ,

$$\bar{\partial}\|\theta^n\|^2 + \|\nabla\theta^n\|^2 \leq C(\|\theta^n\|^2 + R_n), \quad (63)$$

where

$$R_n = \|\rho^{n-1}\|^2 + \tau^2\|\bar{\partial}\tilde{u}^n\|^2 + \|\bar{\partial}\rho^n\|^2 + \|\bar{\partial}\tilde{u}^n - \tilde{u}_t^n\|^2 \quad (64)$$

This implies

$$(1 - C\tau)\|\theta^n\|^2 \leq (1 + C\tau)\|\theta^{n-1}\|^2 + C\tau R_n. \quad (65)$$

For small  $\tau$ , we obtain

$$\|\theta^n\|^2 \leq (1 + C\tau)\|\theta^{n-1}\|^2 + C\tau R_n. \quad (66)$$

By applying this recursively

$$\|\theta^n\|^2 \leq (1 + C\tau)^n\|\theta^0\|^2 + C\tau \sum_{j=1}^n (1 + C\tau)^{n-j} R_j \leq C\|\theta^0\|^2 + C\tau \sum_{j=1}^n R_j. \quad (67)$$

Note we have  $\|\rho^j\| \leq C(\tilde{u})P^{-\frac{k}{d}}$ ,

$$\|\bar{\partial}\rho^j\| = \left\| \frac{1}{\tau} \int_{t_{j-1}}^{t_j} \rho_t ds \right\| \leq C(\tilde{u})P^{-\frac{k}{d}}, \quad (68)$$

$$\|\bar{\partial}\tilde{u}^j - \tilde{u}_t^j\| = \left\| \frac{1}{\tau} \int_{t_{j-1}}^{t_j} (s - t_{j-1})\tilde{u}_{tt}(s) ds \right\| \leq C(u)\tau, \quad (69)$$

$$\tau\|\bar{\partial}\tilde{u}^j\| = \left\| \int_{t_{j-1}}^{t_j} \tilde{u}_t ds \right\| \leq C(\tilde{u})\tau. \quad (70)$$

Collecting the above results, we obtain

$$R_j \leq C(\tilde{u})(\tau + P^{-\frac{k}{d}})^2. \quad (71)$$

This yields

$$\|\theta^n\| \leq C\|\theta^0\| + C(\tilde{u})(\tau + P^{-\frac{k}{d}}) \leq C(\tilde{u})(\tau + P^{-\frac{k}{d}}). \quad (72)$$

Finally, combining this with (72) and (57), we establish the desired result.  $\square$

Now we can give the proof for Theorem 2.

*proof of Theorem 2.* Using the triangle inequality for Lemma 6 and 7, there exists a neural operator  $\mathcal{N}$  such that

$$\begin{aligned} \|\tilde{u}_P^n - u(t_n)\|_{L^2} &\leq \|\tilde{u}_P^n - \tilde{u}^n\|_{L^2} + \|\tilde{u}^n - u(t_n)\|_{L^2} \\ &\leq C(\tau + P^{-\frac{k}{d}}) + C \sup_u \|\mathcal{F}(u) - \mathcal{N}(u)\|_{L^2} T^{1/2} \exp(CLT). \end{aligned}$$

Here we achieve the desired result.  $\square$

We also have the model approximation results, namely, the error between the PDE residual  $\mathcal{R}_P^n(u)$  and the nonlinear term  $\mathcal{F}(u(t_n))$ .

**Lemma 8.** *Assume the solution of problem (1) satisfy  $u_{tt} \in H^k(\Omega)$  and  $\Delta u \in H^k(\Omega)$ . The PDE residual  $\mathcal{R}_P^n(u)$  satisfies*

$$\|\mathcal{R}^n(u) \cdot \Phi_P - \mathcal{F}(u(t_n))\|_{L^2} \leq C(\tau + P^{-\frac{k}{d}}), \quad (73)$$

where  $\Phi_P = (\phi_1, \dots, \phi_P)^T$  and  $\tau = \max_n(t_n - t_{n-1})$ .

*Proof.* We start with the governing equation:

$$u_t(t_n) - D\Delta u(t_n) = \mathcal{F}(u(t_n)).$$

Let  $\Pi_P$  denote the projection onto  $V_P$ , the approximation property ensures that

$$\|(I - \Pi_P)(u_t(t_n) - D\Delta u(t_n))\|_{L^2} \leq CP^{-\frac{k}{d}},$$

since  $u_t, \Delta u \in H^k(\Omega)$ . Using the forward Euler scheme for the time derivative, we have the estimate

$$|(\frac{u(t_n) - u(t_{n-1})}{\tau} - u_t(t_n), \phi_i)| \leq C\tau |(u_{tt}, \phi_i)|.$$

This implies

$$\|\Pi_P(u_t(t_n) - \frac{u(t_n) - u(t_{n-1})}{\tau})\|^2 \leq C\tau \sum_{i=1}^P |(u_{tt}, \phi_i)|^2 \leq C\tau^2 \|u_{tt}(t_n)\|_{L^2}^2.$$

From the definition of  $\mathcal{R}_P^n$ , it follows that

$$\mathcal{R}_P^n \cdot \Phi_P = \Pi_P \left( \frac{u(t_n) - u(t_{n-1})}{\tau} - D\Delta u(t_n) \right).$$

Finally, applying the triangle inequality and combining the results above, we obtain

$$\begin{aligned} \|\mathcal{R}_P^n \cdot \Phi_P - \mathcal{F}(u(t_n))\|_{L^2} &= \|\mathcal{R}_P^n \cdot \Phi_P - (u_t(t_n) - D\Delta u(t_n))\|_{L^2} \\ &\leq \|\mathcal{R}_P^n \cdot \Phi_P - \Pi_P(u_t(t_n) - D\Delta u(t_n))\|_{L^2} + \|(I - \Pi_P)(u_t(t_n) - D\Delta u(t_n))\|_{L^2} \\ &\leq C(\tau + P^{-\frac{k}{d}}). \end{aligned}$$

□

This result shows that our residual term  $\mathcal{R}$  provides a good approximation of the nonlinear term  $\mathcal{F}$ . Consequently, when considering the residual loss  $L^R$  in the optimization process, the trained neural operator  $\mathcal{N}$  can efficiently approximate  $\mathcal{F}$ .

*Remark 6.* In practice, the available data may have limited regularity, such as belonging to  $L^\infty(\Omega)$ . By the Sobolev embedding theorem (Adams & Fournier, 2003), it holds that  $L^\infty(\Omega) \hookrightarrow H^k(\Omega)$  for  $k < \frac{d}{2}$  for  $k < \frac{d}{2}$ , thus we have

$$\|\mathcal{R}^n(u) \cdot \Phi_P - \mathcal{F}(u(t_n))\|_{L^2} \leq C(\tau + P^{-\frac{1}{2} + \xi}), \quad (74)$$

for arbitrary  $\xi > 0$ . For a uniform time step  $\tau = \frac{T}{N}$ , with sufficiently large  $N$  and  $P$ , the error can be made arbitrarily small.

In this way, given data  $\mathcal{R}^n(u)$ , there exists a neural operator  $\mathcal{N}$  such that

$$\|\mathcal{R}^n(u) \cdot \Phi_P - \mathcal{N}(u)\|_{L^2} \leq C(\tau + P^{-\frac{k}{d}}) + C \log(m)^{\frac{1}{2} + P} m^{-\frac{1}{P} \frac{P+2}{P+4}}. \quad (75)$$

## B. Optimization Analysis

To simplify the investigation of the optimization behavior of our method, we consider the following estimates using the one-step absolute squared loss for  $M$  samples:

$$L^D(\theta) := \frac{1}{M} \sum_{i=1}^M \|\beta^1(u_i^1) - \tilde{\beta}^1((\tilde{u}_P^1)_i; \theta)\|_{l^2}^2, \quad (76)$$

$$L^R(\theta) := \frac{1}{M} \sum_{i=1}^M \|\mathcal{R}^1(u_i) - \mathcal{G}(\beta^0((u^0)_i; \theta))\|_{l^2}^2. \quad (77)$$

*proof of Theorem 3.* Without loss of generality, we assume  $D = 1$ . For the first step, we have:

$$\tilde{\beta}^1 = (1 + \tau\Lambda_P)^{-1}(\tilde{\beta}^0 + \tau\mathcal{G}(\tilde{\beta}^0)). \quad (78)$$

Note that the initial condition gives  $\tilde{\beta}^0 = \beta^0$ , we define the function

$$L_i(\theta) = L_i^R(\theta) + L_i^D(\theta) := \|\mathcal{R}_i^1 - \mathcal{G}(\beta_i^0; \theta)\|_{l_2}^2 + \|\beta_i^1 - (1 + \tau\Lambda_P)^{-1}(\beta_i^0 + \tau\mathcal{G}(\beta_i^0; \theta))\|_{l_2}^2 \quad (79)$$

where  $\beta_i^n = \beta^n(u_i^n)$  and  $\mathcal{R}_i^1 = \mathcal{R}^1(u_i^1)$  for  $i = 1, 2, \dots, M$  and  $n = 0, 1$ . The loss function can be rewritten as:

$$L(\theta) = \frac{1}{M} \sum_{i=1}^M L_i(\theta). \quad (80)$$

Consider  $\mathcal{G} : \mathbb{R}^P \rightarrow \mathbb{R}^P$  as a shallow neural network with width  $m$  and examine its behavior under gradient flow with respect to its parameters  $\theta$ , using the loss function  $L(\theta)$ :

$$\frac{d}{ds}\theta(s) = -\nabla_{\theta}L(\theta(s)). \quad (81)$$

The neural Tangent Kernel (NTK) (Jacot et al., 2018) describes the dynamics of this process in the infinite-width limit  $m \rightarrow \infty$ . First, we have:

$$\frac{d}{ds}\mathcal{G}(\beta_i^0; \theta(s)) = -\frac{1}{M}\nabla_{\theta}\mathcal{G}(\beta_i^0; \theta(s))\sum_{j=1}^M\nabla_{\theta}\mathcal{G}(\beta_j^0; \theta(s))^T\partial_{\mathcal{G}}L_j. \quad (82)$$

The standard NTK of  $\mathcal{G}$  for  $\mathbf{x}, \mathbf{y} \in \mathbb{R}^P$  is defined as:

$$\nabla_{\theta}\mathcal{G}(\mathbf{y}; \theta)\nabla_{\theta}\mathcal{G}(\mathbf{x}; \theta)^T \rightarrow \mathbb{E}_{\theta \sim \mu}(\nabla_{\theta}\mathcal{G}(\mathbf{y}; \theta)\nabla_{\theta}\mathcal{G}(\mathbf{x}; \theta)^T) \in \mathbb{R}^{P \times P}. \quad (83)$$

where  $\mu$  denotes the initialization distribution of  $\theta$ .

Note that for a stacked neural network, i.e.,  $\mathcal{G}_i(\mathbf{x}) = \sum_{j=1}^m a_i^j \sigma(\omega_i^j \cdot \mathbf{x} + b_i^j)$ ,  $i = 1, \dots, P$ , we have

$$\mathbb{E}(\nabla_{\theta}\mathcal{G}_i(\mathbf{y})\nabla_{\theta}\mathcal{G}_j(\mathbf{x})^T) = 0, \quad i \neq j.$$

This implies the existence of a function  $\gamma(\mathbf{y}, \mathbf{x}) = \mathbb{E}(\nabla_{\theta}\mathcal{G}_i(\mathbf{y})\nabla_{\theta}\mathcal{G}_i(\mathbf{x})^T)$  since  $\mathcal{G}_i$  are i.i.d. and  $s^* > 0$  such that

$$\frac{d}{ds}\mathcal{G}(\beta_i^0; \theta(s)) = -\frac{1}{M}\sum_{j=1}^M\gamma(\beta_i^0, \beta_j^0)\partial_{\mathcal{G}}L_j. \quad (84)$$

for some  $s \in [0, s^*]$  with high probability (Yang et al., 2025) as  $m \rightarrow \infty$ . For the iteration of the loss function, we have

$$\frac{d}{ds}L(\theta(s)) = \frac{1}{M}\sum_{i=1}^M\partial_{\mathcal{G}}L_i \cdot \frac{d}{ds}\mathcal{G} = -\frac{1}{M^2}\sum_{i,j=1}^M\partial_{\mathcal{G}}L_i\gamma(\beta_i^0, \beta_j^0)\partial_{\mathcal{G}}L_j. \quad (85)$$

Rewriting the right-hand side into matrix form

$$\frac{d}{ds}L(\theta(s)) = -\frac{1}{M^2}e^TKe \quad (86)$$

where  $K \in \mathbb{R}^{MP \times MP}$  and  $e \in \mathbb{R}^{MP}$  are defined as

$$K = I_P \otimes \Gamma, \quad \Gamma = (\gamma(\beta_i^0, \beta_j^0)) \in \mathbb{R}^{M \times M} \quad (87)$$

$$e = (e_1, e_2, \dots, e_P)^T \in \mathbb{R}^{MP} \quad \text{with} \quad e_i = (\partial_{\mathcal{G}_i}L_1, \dots, \partial_{\mathcal{G}_i}L_M)^T \in \mathbb{R}^M. \quad (88)$$



The eigenvalues of  $K$  are determined by those of  $\Gamma$ , which is the NTK of a shallow neural network under an  $L^2$  fitting setup. Its positive definiteness ensures that the minimum eigenvalue,  $\gamma_1 > 0$ , exists (Jacot et al., 2018). Thus we have

$$\frac{d}{ds}L(\theta(s)) \leq -\frac{\gamma_1}{M^2}e^T e = -\frac{\gamma_1}{M^2} \sum_{j=1}^M |\partial_{\mathcal{G}}L_j|^2 \quad (89)$$

Expanding  $\partial_{\mathcal{G}}L_j$  and using the definition of  $\mathcal{R}_j^1$ :

$$\begin{aligned} \partial_{\mathcal{G}}L_j &= -2(\tau(1 + \tau\Lambda_P)^{-1}(\beta_j^1 - (1 + \tau\Lambda_P)^{-1}(\beta_j^0 + \tau\mathcal{G}(\beta_j^0; \theta)) + \mathcal{R}_j^1 - \mathcal{G}(\beta_j^0; \theta)) \\ &= -2(I + \tau(1 + \tau\Lambda_P)^{-1})(\mathcal{R}_j^1 - \mathcal{G}(\beta_j^0; \theta)) \end{aligned} \quad (90)$$

This gives

$$|\partial_{\mathcal{G}}L_j|^2 = 4(\mathcal{R}_j^1 - \mathcal{G}(\beta_j^0; \theta))^T (I + \tau(1 + \tau\Lambda_P)^{-1})^2 (\mathcal{R}_j^1 - \mathcal{G}(\beta_j^0; \theta)). \quad (91)$$

Given that  $L_j = (\mathcal{R}_j^1 - \mathcal{G}(\beta_j^0; \theta))^T (\tau(1 + \tau\Lambda_P)^{-1})^2 (\mathcal{R}_j^1 - \mathcal{G}(\beta_j^0; \theta)) + (\mathcal{R}_j^1 - \mathcal{G}(\beta_j^0; \theta))^T (\mathcal{R}_j^1 - \mathcal{G}(\beta_j^0; \theta))$ , we have

$$\begin{aligned} |\partial_{\mathcal{G}}L_j|^2 &= 4L_j + 8(\mathcal{R}_j^1 - \mathcal{G}(\beta_j^0; \theta))^T (\tau(1 + \tau\Lambda_P)^{-1}) (\mathcal{R}_j^1 - \mathcal{G}(\beta_j^0; \theta)) \\ &\geq 4L_j + 8\frac{\tau(1 + \tau\lambda_P)^{-1}}{(1 + \tau^2(1 + \tau\lambda_1)^{-2})}L_j. \end{aligned} \quad (92)$$

Noting  $L = \frac{1}{M} \sum_{j=1}^M L_j$ , we obtain

$$\frac{d}{ds}L(\theta(s)) \leq -\frac{\gamma_1}{M} \left(4 + 8\frac{\tau(1 + \tau\lambda_P)^{-1}}{(1 + \tau^2(1 + \tau\lambda_1)^{-2})}\right)L. \quad (93)$$

This implies

$$L(\theta(s)) \leq L(\theta(0)) \exp\left(-\frac{\gamma_1}{M} \left(4 + 8\frac{\tau(1 + \tau\lambda_P)^{-1}}{(1 + \tau^2(1 + \tau\lambda_1)^{-2})}\right)s\right). \quad (94)$$

□

*Remark 7.* In the above proof, if we restrict our attention to the single loss  $L^R$  for optimization, the argument parallels the analysis in (90). Specifically, we have

$$\partial_{\mathcal{G}}L_j^R = \mathcal{R}_j^1 - \mathcal{G}(\beta_j^0; \theta) \quad \text{and} \quad |\mathcal{R}_j^1 - \mathcal{G}(\beta_j^0; \theta)|^2 = L_j^R \quad (95)$$

Thus,

$$\frac{d}{ds}L^R(\theta(s)) \leq -\frac{4\gamma_1}{M}L^R. \quad (96)$$

leading to

$$L^R(\theta(s)) \leq L^R(\theta(0)) \exp\left(-\frac{4\gamma_1}{M}s\right), \quad (97)$$

This rate of convergence is slower than that achieved by training with both loss functions  $L$ .

## C. Application to Various Boundary Conditions

### C.1. Inhomogeneous Dirichlet Boundary Condition

For the inhomogeneous Dirichlet boundary condition

$$u = g \quad \text{on } \partial\Omega \times (0, T). \quad (98)$$

we consider harmonic extension of the boundary to obtain  $u_g$ , which satisfies:

$$\begin{cases} -\Delta u_g = 0, & \text{in } \Omega \times (0, T) \\ u_g = g, & \text{on } \partial\Omega \times (0, T) \end{cases} \quad (99)$$

This harmonic extension can be derived using the finite element method. Using  $u_g$ , we reformulate the original problem in terms of  $w := u - u_g$  which satisfies:

$$\begin{cases} w_t - D\Delta w = \mathcal{F}(w + u_g) - (u_g)_t, & \text{in } \Omega \times [0, T] \\ w(x, 0) = w_0(x), & \text{in } \Omega \end{cases} \quad (100)$$

with the initial condition is given by  $w_0(x) = u_0(x) - u_g(x, 0)$ . Since  $w$  satisfies homogeneous Dirichlet boundary condition, we can still use the Laplace eigenfunctions with homogeneous Dirichlet boundary conditions to compute the coefficient  $\tilde{\beta}^n$  of  $w$ . Using  $w$ , we can apply Algorithm 1 to train the neural operator  $\mathcal{N}$ . For the input to the neural operator  $\mathcal{G}$ , the coefficients of  $u_g$  can either be included as part of the input or excluded for training.

## C.2. Neumann Boundary Condition

For the Neumann boundary condition

$$\frac{\partial u}{\partial n} = g. \quad (101)$$

We also consider harmonic extension of the boundary to obtain  $u_g \in L_0^2(\Omega) \cap H^1(\Omega)$ , which satisfies:

$$\begin{cases} -\Delta u_g = 0, & \text{in } \Omega \times (0, T) \\ \frac{\partial u}{\partial n} = g, & \text{on } \partial\Omega \times (0, T) \end{cases} \quad (102)$$

This harmonic extension can be derived using the finite element method. Using  $u_g$ , we reformulate the original problem in terms of  $w := u - u_g$  which satisfies:

$$\begin{cases} w_t - D\Delta w = \mathcal{F}(w + u_g) - (u_g)_t, & \text{in } \Omega \times [0, T] \\ w(x, 0) = w_0(x), & \text{in } \Omega \end{cases} \quad (103)$$

with the initial condition is given by  $w_0(x) = u_0(x) - u_g(x, 0)$ . Since  $w$  satisfies homogeneous Neumann boundary condition, we can still use the Laplace eigenfunctions in  $L_0^2(\Omega)$  with homogeneous Neumann boundary conditions to compute the coefficient  $\tilde{\beta}^n$  of  $w$ . Using  $w$ , we can apply Algorithm 1 to train the neural operator  $\mathcal{N}$ . For the input to the neural operator  $\mathcal{G}$ , the coefficients of  $u_g$  can either be included as part of the input or excluded for training.

## D. Details for Numerical Tests

### D.1. Datasets and Complementary Results

In this section, we provide the details of datasets and some complementary results for the equation we used in Section 3.

#### D.1.1. KPP-FISHER EQUATION

Recall the 1D KPP-Fisher equation on the unit interval:

$$\begin{cases} \frac{\partial u}{\partial t} - \frac{\partial^2 u}{\partial x^2} = u(1 - u), & x \in (0, 1), t \in (0, T] \\ u(x, 0) = u_0(x), & x \in (0, 1) \end{cases} \quad (104)$$

The initial condition  $u_0(x)$  is generated according to  $u_0 \sim \mu$  where  $\mu = \mathcal{N}(0, 49(-\Delta + 7I)^{-2.5})$  with corresponding Dirichlet boundary conditions. We solve the governing equation using an explicit Euler method, employing a piecewise linear finite element method for spatial discretization. The computational domain is discretized on a spatial mesh with a resolution of  $2^{10} = 1024$  and the time step is set to  $\tau = 0.01$ . For the dataset used to train the neural network, data is collected over 10 time steps, using 100 different solutions. For the evaluation and comparison of predicted results, we include 30 time steps.

### D.1.2. ALLEN-CAHN EQUATION

The Allen-Cahn equation is given by:

$$\begin{cases} \frac{\partial u}{\partial t} - \varepsilon^2 \frac{\partial^2 u}{\partial x^2} = W'(u), & x \in (0, 2\pi), t \in (0, T] \\ u(x, 0) = u_0(x), & t \in (0, T) \end{cases} \quad (105)$$

We set  $\varepsilon = 0.1$ . The initial condition  $u_0$  is sampled from the distribution  $\mu = \mathcal{N}(0, 49(-\Delta + 7I)^{-2.5})$  with pure Neumann boundary conditions. An explicit Euler method, with a piecewise linear finite element method for spatial discretization is used. The computational domain is discretized on a spatial mesh with a resolution of  $2^{10} = 1024$  and the time step is set to  $\tau = 0.05$ . For the dataset used to train the neural network, data is collected over 20 time steps, using 100 different solutions. For the evaluation and comparison of predicted results, we include 60 time steps. The training error is given in Table 6.

*Table 6. Errors of the Allen-Cahn equation.*

$E_{L^2}$	$E_{Res}$	$E_{Nonlinear}$
6.58e-04	2.45e-03	6.59e-03

### D.1.3. GRAY-SCOTT EQUATION

The Gray-Scott model is a reaction-diffusion system with two variables,  $A$  and  $S$ , described by the following equations:

$$\begin{cases} A_t - D_A \Delta A = SA^2 - (\mu + \rho)A, & x \in (0, 2\pi)^d, t \in (0, T) \\ S_t - D_S \Delta S = -SA^2 + \rho(1 - S), & x \in (0, 2\pi)^d, t \in (0, T) \\ A(x, 0) = A_0(x) & x \in (0, 2\pi)^d \\ S(x, 0) = S_0(x) & x \in (0, 2\pi)^d \end{cases} \quad (106)$$

where the parameters are set as  $D_A = 2.5 \times 10^{-4}$ ,  $D_S = 5 \times 10^{-4}$ ,  $\rho = 0.04$  and  $\mu = 0.065$ . The initial condition  $A_0$  and  $S_0$  are sampled from the distribution  $\mu = \mathcal{N}(0, 49(-\Delta + 7I)^{-2.5})$  with pure Neumann boundary conditions. An explicit Euler method, with a piecewise linear finite element method for discretization is used. The computational domain is discretized on a spatial mesh with a resolution of  $2^{10} = 1024$  for 1D problems and  $256 \times 256$  for 2D problems. The time step is set to  $\tau = 0.1$ . For the dataset used to train the neural network, data is collected over 20 time steps, using 100 different solutions. For the evaluation and comparison of predicted results, we include 60 time steps. Note that this equation involves two variables, so we include the projection coefficients of both  $A$  and  $S$  as inputs to the neural network.

### D.1.4. SCHRÖDINGER EQUATION

The Schrödinger equation is given by:

$$\begin{cases} u_t - \Delta u + \alpha|u|^2 u + Vu = \lambda u, & x \in (-8, 8)^2, t \in (0, T) \\ u(x, 0) = u_0(x) & x \in (-8, 8)^2 \end{cases} \quad (107)$$

where  $\alpha = 1600$ ,  $\lambda = 15.87$  is the eigenvalue of the steady problem and the potential is defined as:

$$V(x, y) = 100(\sin^2(\frac{\pi x}{4}) + \sin^2(\frac{\pi y}{4})) + x^2 + y^2. \quad (108)$$

The initial condition  $u_0$  is sampled from the distribution  $\mu = \mathcal{N}(0, 49(-\Delta + 7I)^{-2.5})$  with homogeneous Dirichlet boundary conditions. We employ an explicit Euler method for time integration, combined with a piecewise linear finite element method for spatial discretization. The computational domain is discretized on a spatial mesh with a resolution of  $256 \times 256$ . The time step is set to  $\tau = 0.001$ . For the dataset used to train the neural network, data is collected over 20 time steps, using 100 different solutions. For the evaluation and comparison of predicted results, we include 60 time steps. The training error is given in 7.

Table 7. Errors of the Schrödinger equation.

$E_{L^2}$	$E_{Res}$	$E_{Nonlinear}$
9.91e-04	9.37e-03	1.79e-02

### D.1.5. ALZHEIMER’S DISEASE EVOLUTION

We use the gray value of MRI scans as the data and the image is of size  $50 \times 50 \times 50$  and we choose the central part of the image of size  $20 \times 20$  of different  $z$ -location and patient for training and transfer learning, for the time series there are 3 times steps. The training loss curve is displayed in Figure 10. The training error is given in 8. The complementary transfer learning results are shown in Table 9.

Table 8. Accuracy for a selected brain and position.

$1 - L^D (\%)$	$1 - E_{L^2} (\%)$	$1 - E_{Res} (\%)$
98.12	92.23	92.44

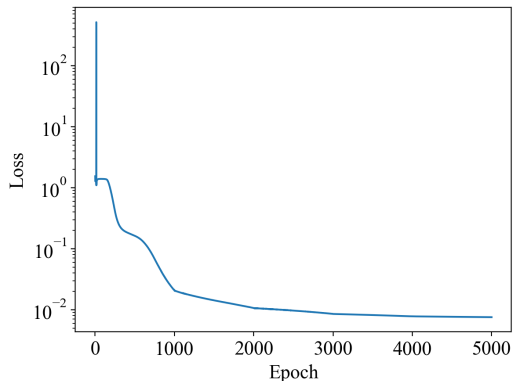


Figure 10. Training loss curve on Alzheimer’s disease evolution.

### D.2. Training Details

We use the Adam optimization method with a full data batch for 5000 epochs, starting with an initial learning rate of  $10^{-3}$ , which is reduced by a factor of 0.25 every 1000 epochs.

### D.3. Neural Network Architecture

We utilize a fully connected neural network for  $\mathcal{N}$  employing the ReLU activation function. The architecture details, including the number of hidden layers and eigenfunctions used in different tests, are summarized in Table 10.

Table 9. Complementary transfer learning accuracy results.

Same brains with different positions			
Location	$1 - L^D$ (%)	$1 - E_{L^2}$ (%)	$1 - E_{Res}$ (%)
1	95.82	91.18	86.20
2	96.02	91.29	81.40
3	95.90	89.10	86.70
4	97.98	89.10	90.00
5	97.88	86.60	92.59
6	96.28	88.40	88.40
7	96.13	89.60	87.70
8	96.28	91.47	85.50
9	95.43	90.96	85.20
10	96.05	92.50	88.00
mean± std	96.62±1.10	90.47± 2.15	88.21±4.27
Different brains with different positions			
Index	$1 - L^D$ (%)	$1 - E_{L^2}$ (%)	$1 - E_{Res}$ (%)
1	98.19	92.19	98.18
2	86.10	83.60	90.70
3	93.15	87.80	90.21
4	98.98	88.10	99.08
5	96.40	85.50	93.18
6	94.15	88.80	85.80
7	98.80	93.21	98.95
8	97.91	92.79	90.28
9	96.10	90.82	90.91
10	96.41	93.53	89.50
mean± std	95.62±3.66	89.63±3.25	92.68±4.33

Table 10. Neural Network Architecture.

Problem	#Eigen function	Neural Network
KPP-Fisher	64	64-1000-64
Allen-Cahn	64	64-1000-64
1D Gray-Scott	64	128-1000-1000-128
2D Gray-Scott	$48^2$	$2 * 48^2$ -1000-1000-1000- $2 * 48^2$
Schrödinger	$64^2$	$64^2$ -1000-1000-1000- $64^2$
Alzheimer’s disease evolution	$16^2$	$16^2$ -16- $16^2$